ACS Combinatorial Science

Research Article

pubs.acs.org/acscombsci

Combinatorial Pulsed Laser Deposition of Fe, Cr, Mn, and Ni-Substituted $SrTiO_3$ Films on Si Substrates

Dong Hun Kim,[†] Lei Bi,[†] Nicolas M. Aimon,[†] Peng Jiang,[†] Gerald F. Dionne,[†,‡] and C. A. Ross*,[†]

[†]Department of Materials Science and Engineering, Massachusetts Institute of Technology, Cambridge, Massachusetts 02139, United States

[‡]Lincoln Laboratory, Massachusetts Institute of Technology, Lexington, Massachusetts 02420, United States

Supporting Information

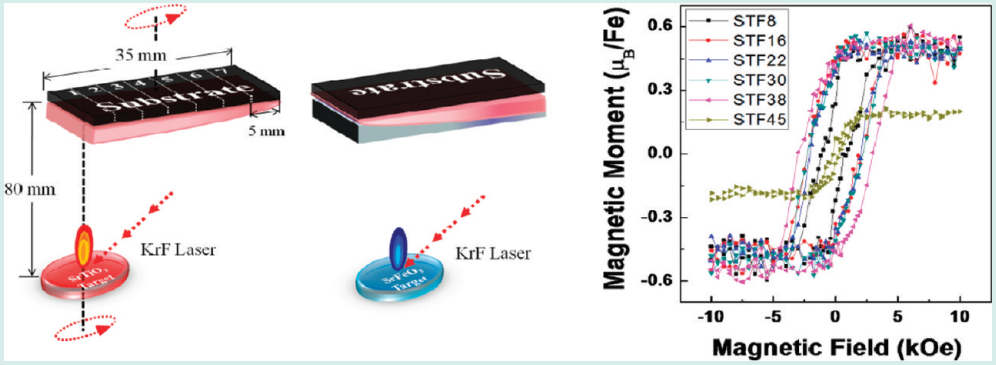

ABSTRACT: Combinatorial pulsed laser deposition (CPLD) using two targets was used to produce a range of transition metal-substituted perovskite-structured $Sr(Ti_{1-x}M_x)O_{3-\delta}$ films on buffered silicon substrates, where M = Fe, Cr, Ni and Mn and x = 0.05−0.5. CPLD produced samples whose composition vs distance fitted a linear combination of the compositions of the two targets. $Sr(Ti_{1-x}Fe_x)O_{3-\delta}$ films produced from a pair of perovskite targets ($SrTiO_3$ and $SrFeO_3$ or $SrTiO_3$ and $SrTi0_{0.575}Fe_{0.425}O_3$) had properties similar to those of films produced from single targets, showing a single phase microstructure, a saturation magnetization of 0.5 μ_B/Fe, and a strong out-of-plane magnetoelastic anisotropy at room temperature. Films produced from an $SrTiO_3$ and a metal oxide target consisted of majority perovskite phases with additional metal oxide (or metal in the case of Ni) phases. Films made from $SrTiO_3$ and Fe_2O_3 targets retained the high magnetic anisotropy of $Sr(Ti_{1-x}Fe_x)O_{3-\delta}$, but had a much higher saturation magnetization than single-target films, reaching for example an out-of-plane coercivity of >2 kOe and a saturation magnetization of 125 emu/cm^3 at 24%Fe. This was attributed to the presence of maghemite or magnetite exchange-coupled to the $Sr(Ti_{1-x}Fe_x)O_{3-\delta}$. Films of $Sr(Ti_{1-x}Cr_x)O_{3-\delta}$ and $Sr(Ti_{1-x}Mn_x)O_{3-\delta}$ showed no room temperature ferromagnetism, but $Sr(Ti_{1-x}Ni_x)O_{3-\delta}$ did show a high anisotropy and magnetization attributed mainly to the perovskite phase. Combinatorial synthesis is shown to be an efficient process for enabling evaluation of the properties of epitaxial substituted perovskite films as well as multiphase films which have potential for a wide range of electronic, magnetic, optical, and catalytic applications.

KEYWORDS: *combinatorial pulsed laser deposition, epitaxial, magnetoelastic, anisotropy*

INTRODUCTION

The perovskite oxides with formula ABO_3 have been studied extensively for applications in electronics such as microelectromechanical systems, actuators, and ferroelectric random access memory devices, and as sensors for magnetic fields or various gases.[1−3] These materials can be easily modified by substitution of a wide range of ions of various sizes and valence states because the perovskite structure can accommodate various substituents by distortion or rotation of the oxygen coordination octahedra. Among the many perovskite oxides, $SrTiO_3$, a wide band gap semiconductor (E_g = 3.2 eV at 0 K), is particularly well studied. $SrTiO_3$ has ferroelectricity, piezoelectricity at low temperature, transparency, and tunability which can be adjusted by applying strain or by doping. Doped $SrTiO_3$ has technologically important properties and is widely used in optical and electronic devices.[4,5] For device fabrication it is useful to grow perovskite films onto Si to take advantage of the existing Si process infrastructure, but in general, perovskite films are polycrystalline when grown directly onto Si,[6] so to obtain epitaxial films, a buffer layer is employed.[7−9] A range of transition metals, including Fe, Co, Ni, and Cr, have been substituted on the B sites, and in certain cases this leads to a material with room temperature ferromagnetic and magneto-optical properties,[10−13] which may be useful in optical or

Received: July 19, 2011
Revised: January 5, 2012
Published: February 21, 2012

 © 2012 American Chemical Society

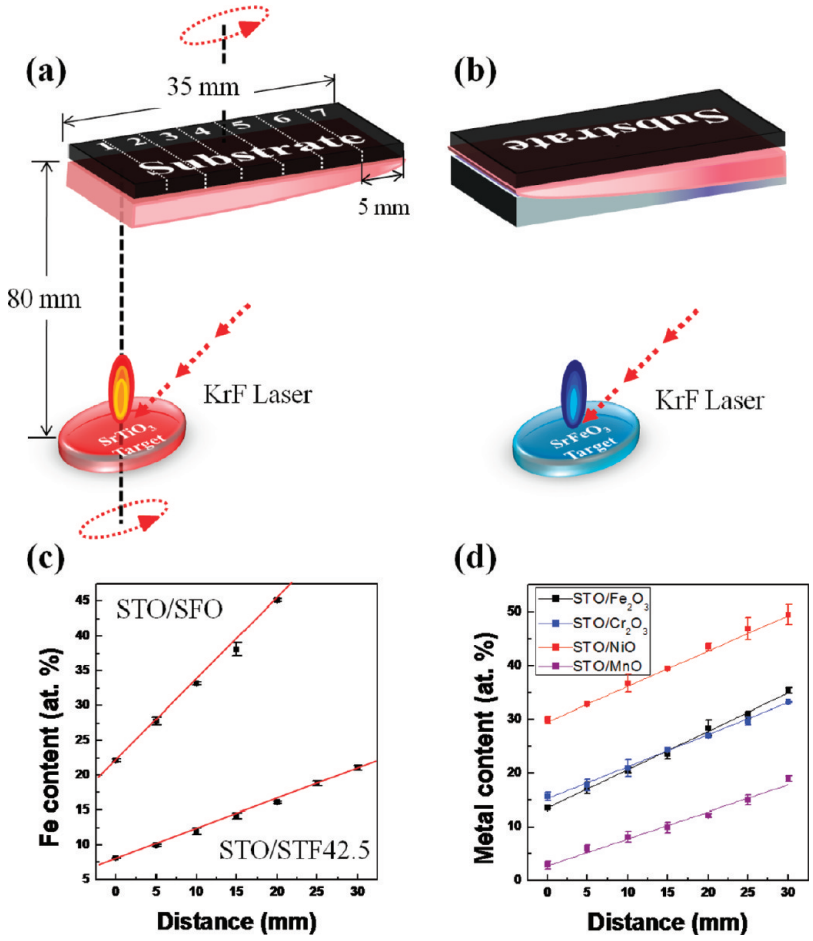

Figure 1. Schematic diagram illustrating the preparation process of $Sr(Ti_{1-x}Fe_x)O_{3-\delta}$ thin films by combinatorial pulsed laser deposition. (a) Deposition of $SrTiO_{3-\delta}$ thin film, (b) deposition of $SrFeO_{3-\delta}$ thin film after rotating the substrate. (c) Fe contents expressed as Fe/(Ti + Fe) as a function of substrate position from the STO-rich to the STF42.5 or SFO-rich ends of the substrate. (d) Metal composition as a function of substrate position from the STO-rich to the metal oxide-rich ends of the films. Compositions at each position were determined by WDS.

spintronic devices. A comparison of magnetic properties of a variety of transition metal-substituted $SrTiO_3$ materials is given in the Supporting Information.

Pulsed laser deposition (PLD) is a convenient method for synthesizing films of complex oxides, including the ability to make nonequilibrium structures with controlled lattice strain.[14] Exploration of a wide composition space is considerably simplified by the use of combinatorial synthesis methods, in which a spread of compositions is formed simultaneously during one deposition. This avoids the need to make a large number of targets of different compositions, and ensures that all samples are made under comparable conditions of temperature, pressure, and other process variables. Combinatorial PLD (CPLD) has been employed to make a wide range of materials systems, including transparent conducting oxides and complex transition metal oxides such as high-*k*, colossal magnetoresistance, thermoelectric, magnetic, or multiferroic materials.[15−18] Composition variation is usually carried out using complicated instrumentation including shutters, moving masks, or dual laser beams. A simpler method is to arrange the target geometry to create a thickness gradient by offsetting the positions of the target and substrate. Deposition is carried out from two targets sequentially, producing submonolayer films from each target to ensure intermixing of the film. However, there has been little work reported on this process and on comparing the properties of films grown by CPLD with those made from single targets.

In this work, we use CPLD to synthesize films of $SrTiO_3$ containing Fe, Mn, Ni, and Cr on CeO_2/YSZ buffered Si. The $Sr(Ti_{1-x}Fe_x)O_{3-\delta}$ (STF) system, which shows a continuous solid solution between the $SrTiO_3$ and $SrFeO_3$ end members, has been the focus of intense interest since first being synthesized by Clevenger.[19] At a low Fe content, the Fe acts as an acceptor and makes STF a good electronic conductor. At higher Fe content, STF is an ionic conductor.[20,21] Substitution of Fe for Ti results in a systematic decrease in band gap and an increase in electron, hole, and oxygen vacancy concentration.[22] We have shown that STF films with <50% Fe deposited in vacuum epitaxially on buffered Si substrates exhibit room-temperature ferromagnetism with a strong out-of-plane magnetic anisotropy that results from the presence of magnetoelastic Fe^{2+} and Fe^{4+} ions and the compressive in-plane lattice strain.[10,13]

Similarly to Fe, Cr and other transition metals can be introduced onto the B-sites of STO. We found that $Sr(Ti_{1-x}Co_x)O_{3-\delta}$ (STC) films also exhibit room temperature ferromagnetism and a magnetoelastic anisotropy, while $Sr(Ti_{1-x}Cr_x)O_{3-\delta}$ (STCr) is not ferromagnetic. The predominant Cr^{3+} ions present in STCr deposited in high vacuum are not magnetoelastic, so there is no magnetoelastic stabilization of the magnetism in STCr at room temperature. Although there

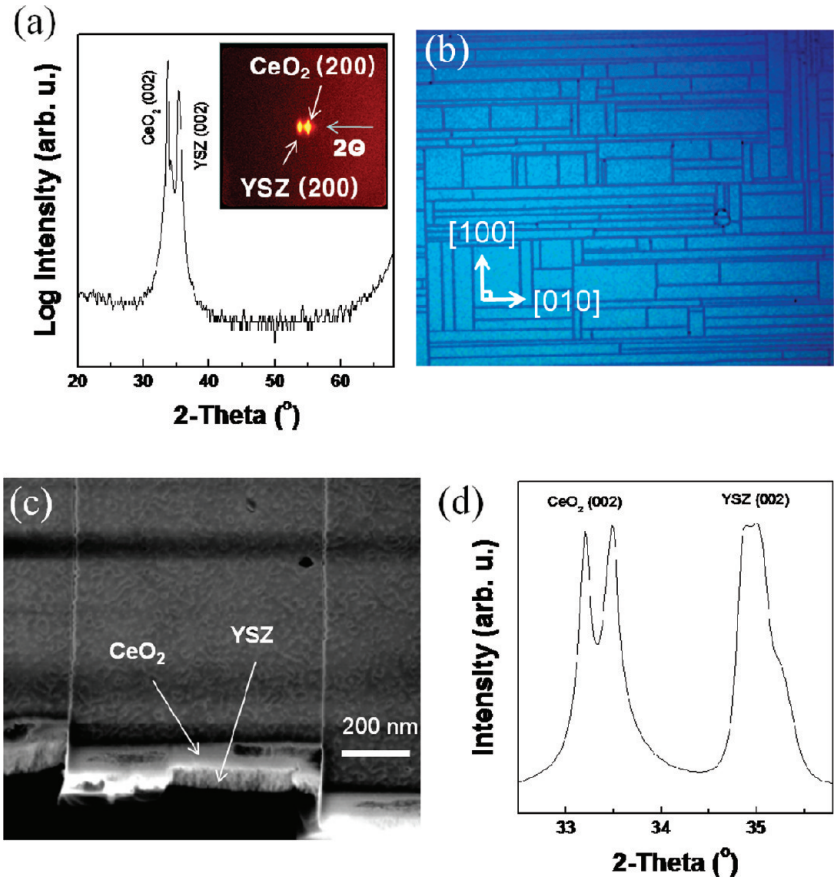

Figure 2. (a) θ-2 θ scan of CeO_2 (120 nm)/YSZ (120 nm) buffer layer on Si substrate. The inset is the two-dimensional XRD spectrum of CeO_2 (120 nm)/YSZ (120 nm) buffer layer on Si substrate. (b) Optical microscope image of 180 nm CeO_2/180 nm YSZ with 500× magnification. (c) Tilted SEM image of 180 nm CeO_2/180 nm YSZ thin films on Si substrate. (d) XRD pattern of 180 nm CeO_2/180 nm YSZ on Si substrate.

has been some examination of ferromagnetism in Mn- or Ni-substituted STO[12,23,24] (STM and STN), the relation between the magnetism and the structure and valence states of the ions is still incomplete. This article describes the microstructure, phases present, and magnetic properties of epitaxial STF, STM, STCr, and STN on buffered Si as a function of film composition which is determined by the end-member targets used in the CPLD synthesis. We show that films made from perovskite targets are single phase perovskite, but films made from a STO target and a binary oxide target can also contain nonperovskite phases. Single phase perovskite films have properties similar to those made from a single target, while the two-phase films can show interesting properties such as an enhanced moment and anisotropy.

■ EXPERIMENTAL PROCEDURES

Disk-shaped 2.5 cm diameter $SrTiO_3$ (STO), $SrFeO_3$ (SFO), and $Sr(Ti_{1-x}Fe_x)O_3$ (x = 0.05, 0.1, 0.2, 0.35, 0.4, 0.425, 0.45, and 0.5, described respectively as STF5, STF10, STF20, STF35, STF40, STF42.5, STF45, and STF50) targets were prepared by a conventional mixed oxide method. The mixtures of powders were calcined at 1250 °C for 3 h and sintered at 1400 °C for 5 h. Fe_2O_3, Cr_2O_3, MnO, and NiO targets were purchased from Plasmaterials (CA). The Si (100) substrates were ultrasonically cleaned sequentially in trichloroethylene, acetone, and isopropyl alcohol to remove organic materials and rinsed with deionized water. To obtain high quality perovskite thin films on Si, yttria-stabilized zirconia (YSZ) and CeO_2 bilayers were used as a buffer layer. The YSZ and CeO_2 layers were deposited by PLD using a KrF excimer laser of 248 nm of wavelength under oxygen pressure of 0.4 mTorr and 5 mTorr, respectively at 800 °C substrate temperature, a fluence of 2.5 J/cm^2, and 5.5 cm distance between target and substrate.

STF thin films were deposited by combinatorial PLD on CeO_2/YSZ buffered Si substrates as shown in Figure 1 (a) and (b). The STF thin films are formed by repeated alternating deposition of the first layer (STO in Figure 1) at 0° and the second layer (e.g., SFO) at 180° substrate rotation position. This sequence is repeated until the desired thickness is obtained. The rotation axis of the substrate is offset compared to the target center to obtain a thickness gradient and a compositionally graded thin film. First, each target was ablated without substrate rotation to calculate the deposition rate. The deposition rates of STO, STF42.5, and SFO thin films were almost the same (40 nm per 10,000 laser pulses at the thickest part of the film). The targets were ablated with 100 pulses during each of 100 cycles to obtain approximately one unit cell of each material directly above the target on each cycle. Films were deposited to a total thickness of approximately 80 nm along the length of the sample (25 or 35 mm). The deposition rate of Fe_2O_3, Cr_2O_3, MnO, and NiO was lower than that of STO. The thicknesses from 20,000 pulses were 80, 44, 36, 25, and 45 nm for STO, Fe_2O_3, Cr_2O_3, MnO, and NiO, respectively. In CPLD growth involving these targets, the films were built up using cycles consisting of 100 pulses on each

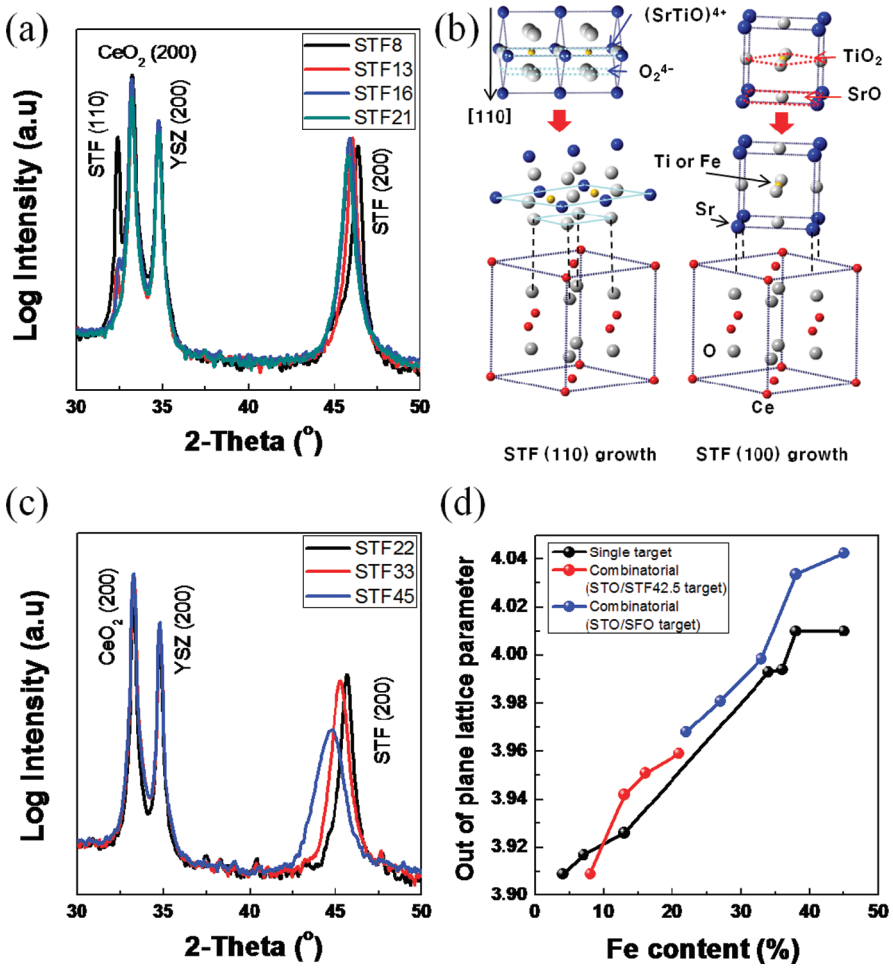

Figure 3. (a) XRD patterns of STF thin films deposited by CPLD from STO and STF42.5 targets. (b) Schematic configuration of STF thin films on a CeO_2 layer showing growth of STF (110) (left) and STF (100) (right). (c) XRD patterns of CPLD STF thin films from STO and SFO targets. (d) Out-of-plane lattice parameter as a function of Fe content.

target. This leads to a lower content of Fe, Cr, Mn, or Ni and higher Ti content compared to the STO/STF CPLD case.

X-ray diffraction (XRD: Rigaku D/MAX-R, λ=1.5406 Å) and two-dimensional XRD (2DXRD: Bruker D8 with General Area Detector Diffraction System) were used to identify the phases present and to measure lattice parameters. Magnetic properties were measured by vibrating sample magnetometer (VSM: ADE model 1660) at room temperature. Film composition was probed using wavelength dispersive X-ray spectroscopy (WDS). Microstructure was analyzed by scanning electron microscopy (SEM: Helios Nanolab 600). The valence state of the elements was investigated by X-ray photoelectron spectroscopy (XPS) using a Kratos AXIS Ultra imaging spectrometer with a monochromatic Al Kα radiation source. Surface morphologies were measured using an atomic force microscope (AFM: Veeco/Digital Instruments Nanoscope IIIa controller with Dimension 3000 Scanning Probe Microscope). The ferromagnetic domain structures were investigated on out-of-plane alternating current (a.c.)-demagnetized samples using magnetic force microscopy (MFM: Veeco/Digital Instruments Nanoscope) using a cobalt/chromium coated tip over an area of 2 μm × 2 μm.

RESULTS AND DISCUSSION

1. CeO_2/YSZ Buffer Layers. A YSZ/CeO_2 bilayer buffer layer was used to enable integration of the CPLD perovskite films onto silicon substrates. The buffer layers were grown by conventional PLD from single targets. Buffer layers with 120 nm of CeO_2/120 nm of YSZ grew epitaxially as shown in Figure 2(a). Only two peaks corresponding to the (200) peaks of CeO_2 and YSZ were observed around 33.1° and 34.9°, respectively, consistent with a high quality epitaxial film structure. There were no peaks other than (h00), nor peaks from secondary phases. The full width at half-maximum (fwhm) of the CeO_2 (200) diffraction peak produced from the θ-rocking curve was 0.735 ± 0.005°. The out-of-plane lattice parameter of CeO_2 (120 nm) and YSZ (120 nm) films was 5.398 Å and 5.143 Å, respectively, similar to the bulk value (5.41 Å for CeO_2 and 5.14 Å for YSZ).[25]

Two dimensional XRD (inset) showed spot-like diffraction patterns indicating that CeO_2/YSZ formed epitaxial layers with respect to the (100) Si substrate. As the thickness of the buffer layers increased the out-of-plane lattice parameter of YSZ increased. The out-of plane lattice parameter of YSZ for 30 nm CeO_2/30 nm YSZ, 60 nm CeO_2/60 nm YSZ, and 120 nm CeO_2/120 nm YSZ stacks was 5.114 Å, 5.135 Å, and 5.143 Å (close to bulk), respectively. We observed rectangular cracks in the 180 nm CeO_2 /180 nm YSZ film, seen in Figure 2 (b).

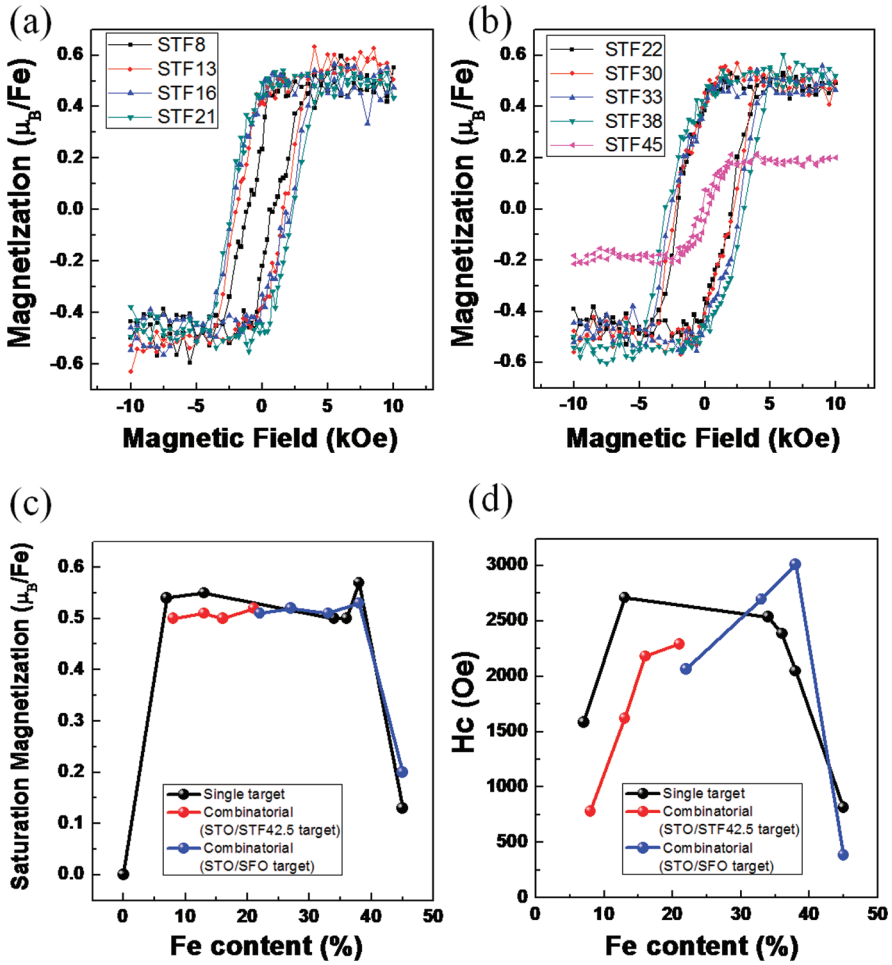

Figure 4. (a) Out-of-plane magnetic hysteresis of STF thin films deposited by CPLD from STO and STF42.5 targets. (b) Out-of-plane magnetic hysteresis of STF thin films from STO and SFO targets. (c) Saturation magnetic moment of STF thin films prepared by CPLD and from single targets as a function of Fe content. (d) The coercivity of STF thin films as a function of Fe content.

When the YSZ thickness exceeded a critical thickness, thermal cracks developed because of the thermal expansion difference between Si ($\alpha_{Si} = 4.5 \times 10^{-6}$ K^{-1} at 1100 K) and YSZ ($\alpha_{YSZ} = 10.9 \times 10^{-6}$ K^{-1} at 1100 K).[26,27] The YSZ film developed a thermal tensile stress during cooling and cracked along both [100] and [010] directions, with the cracks propagating into the CeO_2 layer, Figure 2(c).

In the CeO_2 layer, the out-of-plane lattice parameter increased with increasing thickness, having values of 5.374 Å, 5.382 Å, and 5.398 Å for 30 nm CeO_2/30 nm YSZ, 60 nm CeO_2/60 nm YSZ, and 120 nm CeO_2/120 nm YSZ stacks, respectively, indicating increasing in-plane compressive lattice strain. The thermal expansion is $\alpha_{CeO2} = 13.5 \times 10^{-6}$ K^{-1} at 1100 K, similar to YSZ. Above a critical thickness the (200) peak of CeO_2 split, as illustrated in Figure 2 (d) for 180 nm CeO_2 /180 nm YSZ on Si, indicating partial strain relaxation.[28] On the basis of these results, a buffer layer thickness of 120 nm CeO_2 and 120 nm YSZ was selected, which does not exhibit cracking or peak splitting.

2. STF Films from STO and STF Targets. Eighty nanometer thick films of STF were grown by CPLD from two target pairs: STO/SFO and STO/STF42.5. The substrate temperature was 650 °C, laser fluence of 1.3 J/cm^2, distance between target and substrate 8 cm, and pressure was 2×10^{-6} Torr. For comparison, STF thin films were deposited from single targets under the same conditions. Each CPLD sample was cut into 5 mm ×5 mm pieces for analysis. The 25 mm long STO/SFO sample was cut into five samples of average composition $Sr(Ti_{0.78}Fe_{0.22})O_{3-\delta}$, $Sr(Ti_{0.73}Fe_{0.27})O_{3-\delta}$, $Sr(Ti_{0.67}Fe_{0.33})O_{3-\delta}$, $Sr(Ti_{0.62}Fe_{0.38})O_{3-\delta}$, and $Sr(Ti_{0.55}Fe_{0.45})O_{3-\delta}$, while the 35 mm long STO/STF42.5 yielded compositions of $Sr(Ti_{0.92}Fe_{0.08})O_{3-\delta}$, $Sr(Ti_{0.90}Fe_{0.10})O_{3-\delta}$, $Sr(Ti_{0.87}Fe_{0.13})O_{3-\delta}$, $Sr(Ti_{0.86}Fe_{0.14})O_{3-\delta}$, $Sr(Ti_{0.84}Fe_{0.16})O_{3-\delta}$, $Sr(Ti_{0.81}Fe_{0.19})O_{3-\delta}$, and $Sr(Ti_{0.79}Fe_{0.21})O_{3-\delta}$, where δ represents the oxygen deficiency (not measured). The relation between Fe content calculated as Fe/(Ti + Fe) × 100 at. % and substrate position d is shown in Figure 1 (c). In these systems, Fe substitutes into the Ti sites and the Fe content increased linearly along the sample. The relation between composition and distance was fitted by

$$C_f = 0.22 \times C_1 + C_2 \times (120d + 1)$$

where C_f is the Fe content in the film, C_1 and C_2 are the Fe contents of films deposited from the two targets ($C_1 = 0$ for the STO target, $C_2 = 36$ at.% for STF42.5, and 100 at.% for SFO), and d is the distance from the center of the first sample in mm. The extrapolated x-axis intercept values are almost the same for both series, −19.2 and −19.4 mm for STO/STF42.5 and STO/SFO, respectively. The slopes of the composition vs d for STO/STF42.5 and STO/SFO were 0.413 and 1.145, respectively, equal to $(C_1 + C_2) \times 0.01145$. This result indicates that the film

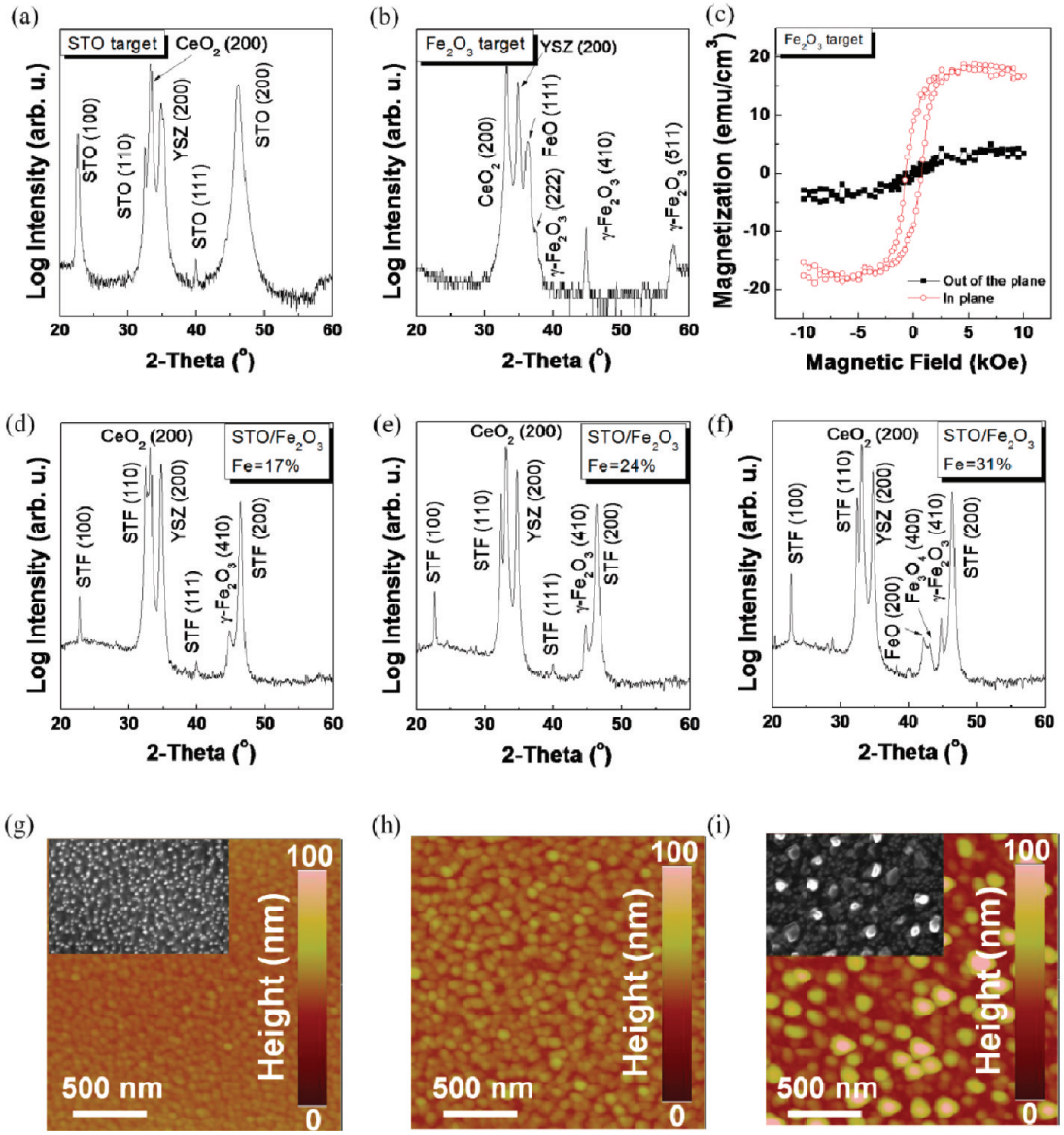

Figure 5. (a) XRD pattern of STO films on CeO_2/YSZ buffered Si substrate deposited at 650 °C and 2×10^{-6} Torr. (b) XRD pattern of Fe_2O_3 films on CeO_2/YSZ buffered Si substrate deposited at the same condtions. (c) Magnetic hysteresis curve of Fe_2O_3 films measured at room temperature. (d), (e), and (f) are XRD patterns of the second (Fe = 17%), fourth (Fe = 24%), and sixth (Fe = 31%) films starting from STO-rich end of the CPLD sample fabricated from STO and Fe_2O_3 targets. (g), (h), and (i) show the surface morphology of each film with an area of 2×2 μm^2. The insets in (g) and (i) are top view SEM images of the same films fabricated from STO and Fe_2O_3 targets with the same scale as the AFM image.

composition can be modeled as a linear combination of the end members.

Figure 3a shows the XRD patterns of STF thin films fabricated from STO/STF42.5. Only perovskite peaks were present. In this range of Fe content, the films grew either as single crystal films with (100) orientation, or as "double epitaxial" films which consist of (110)-oriented nanopillars in a (100) matrix as shown in our prior work.[29] STF films of low Fe content had a large (110) diffraction peak and the intensity of the (110) peak decreased with Fe content. At x = 21% the (110) peak disappeared indicating a transition to single-crystal growth. This result is similar to that of films deposited from a single target. The double-epitaxial growth is believed to form to relieve strain, and its growth was influenced by the surface energy of the (110) facet with respect to (100). Although the (110) plane of STO had a larger lattice mismatch with the substrate compared to the (100) plane, the (110) growth was promoted on the polar CeO_2 surface at low Fe content because the [110] direction consisted of charged layers of $(SrTiO)^{4+}$/$(O_2)^{4-}$ (left panel of Figure 3b). However, as the Fe content increased, the films deposited under reducing conditions (2×10^{-6} Torr in this study) contained many oxygen vacancies which reduced the polarity of the (110) plane, so (100) was favored (right panel of Figure 3b). Films deposited from STO/SFO targets lacked a (110) peak, Figure 3c, and the (200) peak became broader and less intense as the Fe content increased to 45%.

The STF (200) peaks shifted to lower angles with increasing Fe content indicating an increase in out of plane lattice parameter with Fe content (Figure 3d). According to XPS analysis, Fe ions in the STF films were present in Fe^{2+}, Fe^{3+}, and Fe^{4+} valence states to compensate for the oxygen vacancies which resulted from deposition under reducing conditions. The low valence state ions had a larger ionic radius than the Ti^{4+}

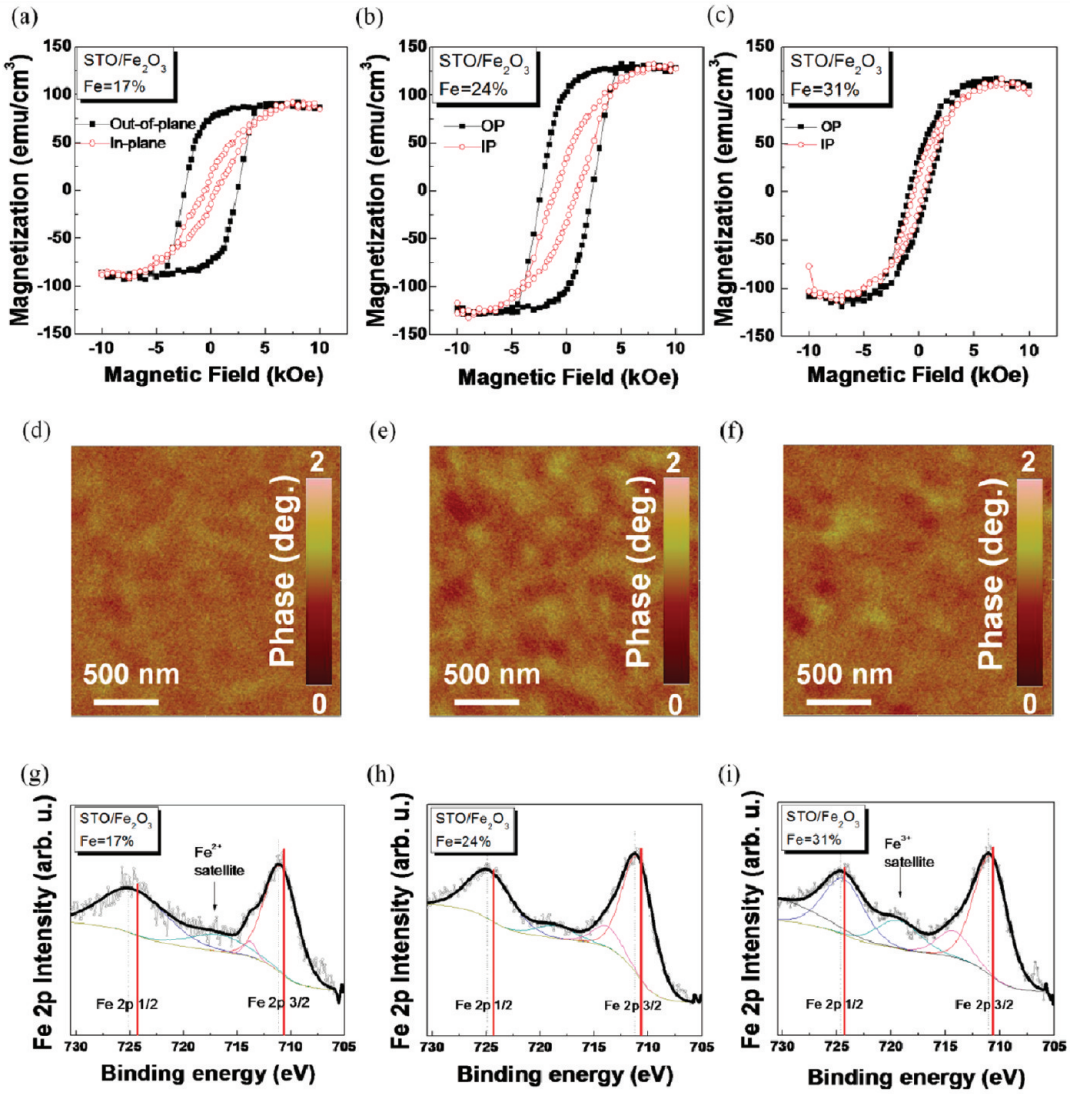

Figure 6. In-plane and out-of-plane magnetic hysteresis curves of the second (a, Fe = 17%), fourth (b, Fe = 24%), and sixth (c, Fe = 31%) films from STO and Fe_2O_3 targets. (d), (e), and (f) are the MFM images of each film. (g), (h), and (i) are Fe 2p XPS spectra of the same films.

which they replaced (Fe^{2+} 0.780 Å, Fe^{3+} 0.645 Å, Ti^{4+} 0.605 Å), increasing the in-plane compressive lattice strain in the films. The in-plane lattice parameters of STF thin films measured by high resolution XRD reciprocal space mapping were almost the same as the spacing of the (220) planes of the CeO_2. For comparison, the lattice parameters of thin films deposited from single targets are shown in Figure 3d. The out-of-plane lattice parameters of thin films from single targets also increased as Fe content increases but were generally slightly smaller than those of the films made by CPLD. This may indicate a difference in average Fe valence state for films of the same composition made by single-target vs combinatorial PLD, which could come from differences in the plume or incidence angle of the arriving species. The lattice parameters showed the most difference at compositions of 45%. This is attributed to the formation of a Fe_2O_3 peak in films deposited from a single target, whereas there was no Fe_2O_3 peak in the film deposited by the combinatorial method.

Figure 4a and b show the out-of-plane magnetic hysteresis loops of STF films deposited from STO/STF42.5 targets (Figure 4a) and STO/SFO targets (Figure 4b). All the films in the range $0.08 \leq x \leq 0.38$ had an out-of plane easy axis and showed a similar saturation magnetic moment (M_s) of ~0.5 μ_B/Fe, except for STF45 which has a lower M_s of ~0.2 μ_B/Fe, Figure 4c. (For reference, 0.5 μ_B/Fe corresponds to a magnetization of 27 emu/cm^3 at 33% Fe.) The abrupt decrease of M_s and anisotropy at $x = 0.45$ was also seen for the STF45 film deposited from a single target. The coercivity H_c was high, reaching 3000 Oe, but also dropped abruptly at 45% Fe (Figure 4d). The high anisotropy and out-of-plane easy axis are attributed to magnetoelastic effects, as reported earlier for films deposited from single targets.[13] The decrease in anisotropy and magnetization at high Fe content are assumed to result from a decrease in film strain as the film relaxed, and also to the development of antiferromagnetic exchange coupling at high Fe doping content because the probability of nearest-neighbor Fe ions increased with Fe content. The coercivity H_c was dominated by magnetoelastic anisotropy and followed the strain state, decreasing at 45% Fe along with M_s and magnetic anisotropy. The strain-relaxed film was easier to switch, in agreement with Gan et al.[30]

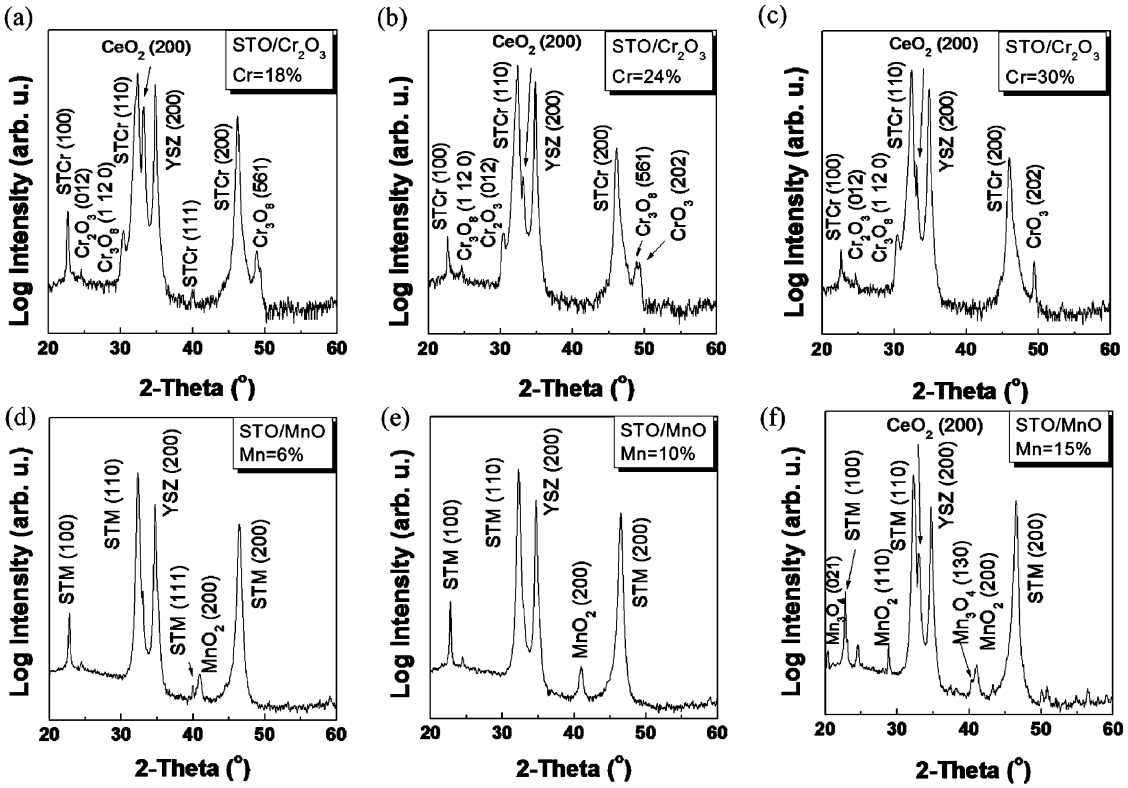

Figure 7. XRD patterns of films made by CPLD from STO/Cr_2O_3 targets ((a), (b), and (c)) and from STO/MnO targets ((d), (e), and (f)).

3. STF Films from STO and Fe_2O_3 Target. The prior section described samples fabricated from perovskite targets to make a single-phase stoichiometric perovskite film. However, it is also possible to fabricate transition metal-substituted STO thin films with CPLD using targets of different crystal structure. Figure 1d shows the composition of films made from STO/Fe_2O_3, STO/Cr_2O_3, STO/MnO, and STO/NiO targets. The transition metal (TM) content calculated as (TM/TM + Ti) increased linearly with distance along the sample, though with a smaller gradient compared to the STO/STF series.

Figure 5 shows the XRD patterns of the STO/Fe_2O_3 combinatorial and end-member films on CeO_2/YSZ buffer layers. Figure 5a shows data from a film made just from the STO target (without substrate rotation), which was a polycrystalline perovskite film with out-of-plane lattice parameter 3.936 Å based on the (100) and (200) peaks, and 3.907 Å based on the (110) and (111) peaks, larger than bulk 3.905 Å presumably because of the presence of oxygen vacancies. Figure 5b shows data from a film made from the Fe_2O_3 target in vacuum, containing mixed phases of rocksalt-structure FeO (wustite) and spinel-structure γ-Fe_2O_3 (maghemite) or Fe_3O_4 (magnetite). Figure 5c shows its magnetic hysteresis loop, which exhibited an in-plane easy axis as seen earlier in γ-Fe_2O_3 films.[31] The relatively low saturation magnetization (20 emu/cm^3, about 5% of that of maghemite) is due to the predominance of antiferromagnetic FeO, and the in-plane anisotropy is due to the shape of the film. Hematite (α-Fe_2O_3) was not observed; prior work showed that growth in a vacuum favors formation of maghemite over hematite, while hematite is promoted in ambient oxygen.[32]

Figure 5 panels d, e, and f show the XRD patterns of the second, fourth, and sixth pieces cut from the STO/Fe_2O_3 CPLD sample, with average compositions of 17%, 24% and 31% Fe, along with AFM images with an area of 2 μm × 2 μm, Figure 5 panels g, h, and i. The insets in Figure 5 panels g and h are SEM images of the films with 17% and 31% Fe, respectively. These films were predominantly perovskite structure (100)+(110) oriented STF with spinel (labeled as γ-Fe_2O_3) peaks present in an amount that increased with Fe content. The two-phase film grew because the ratio of Sr/(Ti + Fe) in the arriving flux was smaller than the ratio of 1:1 required to form pure STF, and occupancy of the A sites of the perovskite is disfavored by the small size of the Fe ions. As Fe content increased the intensity of the (h00) peaks increased while the (110) peaks decreased. The lower Fe content films, with smallest iron oxide peaks, had a low roughness (R_{rms} = 1.5 nm) whereas the 31% Fe sample was significantly rougher (R_{rms} = 15.5 nm). Spinel peaks appeared first at low Fe contents, thereafter, FeO peaks appeared as the Fe content increased, but it was difficult to determine the exact proportions of STF, γ-Fe_2O_3, or Fe_3O_4, and FeO phases from the XRD data.

The appearance of FeO was associated with abrupt roughening of the surface morphology and a decrease in the STF out-of-plane lattice parameter, from 3.919 Å to 3.910 Å as Fe content changed from 13% to 35%. The in-plane lattice parameters extracted from the (112) peaks measured using 2D-XRD increased from 3.877 Å to 3.896 Å as the Fe content changed from 13% to 35%. All the films were therefore tetragonally distorted, that is, the c/a ratio was larger than 1, where c is the out-of-plane and a is in-plane lattice parameter. However, the tetragonality (c/a = 1.011 for 13% Fe and 1.003 for 35%Fe) was less than that of films deposited from a single target. The difference is attributed to strain relaxation enabled by the growth of γ-Fe_2O_3 and FeO. At 35% Fe content film the strain was almost fully relaxed.

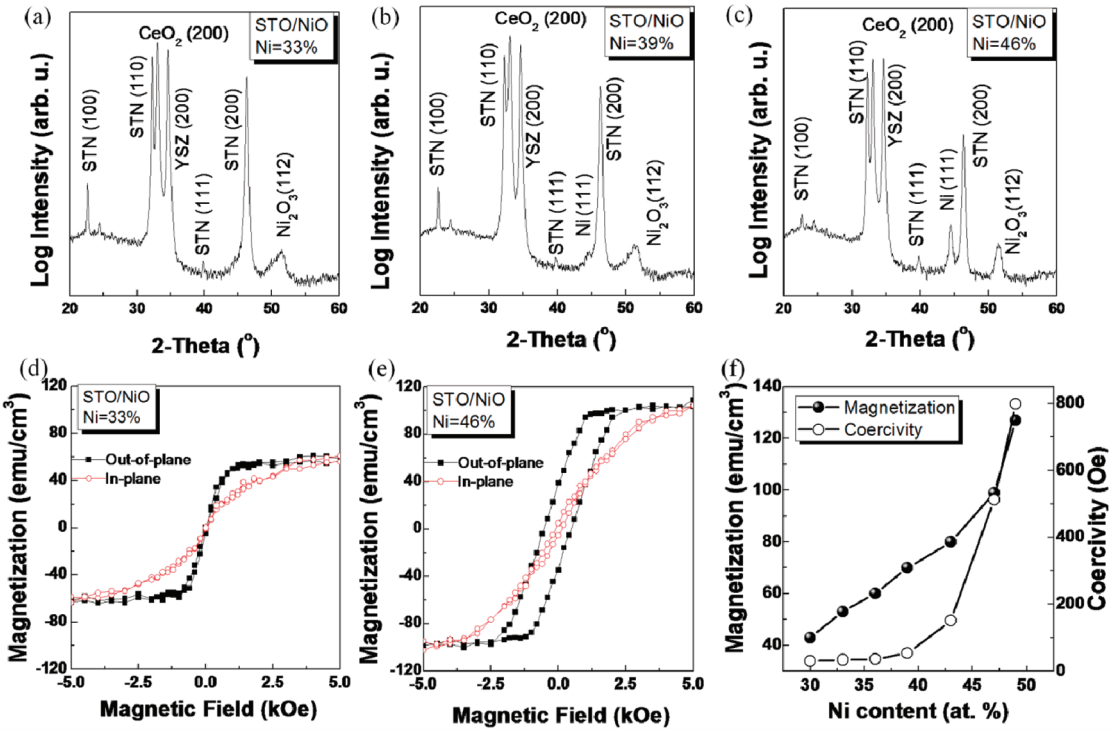

Figure 8. XRD patterns of CPLD thin films from STO/NiO targets having Ni contents of 33% (a), 39% (b), and 46% (c). (d), and (e) show in-plane and out-of-plane magnetic hysteresis curves of the 33 and 46% Ni samples, respectively. (f) Magnetization and coercivity of the films as a function of Ni content.

Figure 6 panels a, b, and c show the in-plane and out-of-plane magnetic hysteresis of the three samples. Those with 17% and 24% had hysteresis loops which resembled those of single-phase STF films, with an out-of-plane anisotropy due to magnetoelastic effects from the tetragonal distortion of the unit cell. The decrease in out-of-plane anisotropy followed the decrease in the c/a ratio of the films, and the film with x = 31% was almost anisotropic, corresponding to its c/a ratio of 1.003. The anisotropy was therefore consistent with the magnetoelastic effects seen in STF films grown from perovskite targets, and inconsistent with the existence of metallic Fe clusters which would have little or no anisotropy.

The saturation magnetization of the films was notably higher than what was found in single-phase STF films of the same composition by a factor of about 7 in the composition range 13% to 28% Fe. For example, the dual-phase film with average 24% Fe had M_s = 125 emu/cm^3 whereas single-phase STF with 24% Fe had M_s = 20.5 emu/cm^3. This high magnetization is attributed to the spinel component of the films, whose bulk magnetization is 420 emu/cm^3 for maghemite or 480 emu/cm^3 for magnetite. Although these phases are typically magnetically soft, the hysteresis loops show that the two-phase films reversed collectively, without any low-field steps. This may be indicative of an exchange-spring behavior[33,34] whereby the softer, higher-moment spinel component reversed cooperatively with the higher-anisotropy STF because of exchange coupling between the phases. The result is interesting in enabling the high anisotropy of the STF to be maintained while increasing the net magnetization of the film. Figure 6 panels d, e, and f show magnetic force microscope (MFM) images of each sample after a.c.-demagnetization. The images show out of plane magnetic domains ~100 nm across, but their locations did not correspond to the peaks of the film topography.

XPS analysis was carried out to investigate the Fe valence state (Figure 6 panels g, h, and i). The Fe 2p 2/3 and 2p 1/2 doublets marked with a dash occurred at 711.2 and 725.3 eV, respectively, for the 17% thin film and moved to slightly lower energies as Fe content increased. These peaks were located at a high binding energy compared to Fe^{3+} in Fe_2O_3 marked by the red line (710.7 and 724.3 eV for Fe 2p 2/3 and 2p 1/2, respectively).[35] The peak shift indicates the existence of Fe^{4+} ions.[36,37] Though it was difficult to quantify the proportions of each Fe valence state, the Fe^{2+} peak was relatively stronger at x = 17%, but the 719 eV Fe^{3+} satellite increased with x, showing that the proportion of Fe^{3+} increased as the Fe content increased. The dominance of Fe^{3+} at x = 35% also contributed to the lower magnetic anisotropy because Fe^{3+} in an octahedral site is not a magnetoelastic ion.

4. STCr and STM Films from STO and Cr_2O_3 or MnO Targets. Figure 7 panels a, b, and c exhibit the XRD patterns of three samples fabricated by CPLD using STO and Cr_2O_3 targets, that is, the second (Cr 18%), fourth (Cr 24%), and sixth (Cr 30%) samples counting from the STO-rich end of the substrate. All the films had perovskite structures with small proportions of various chromium oxide phases. Cr_2O_3 and Cr_3O_8 peaks were present around 24.5 and 30.4° in films with low Cr contents, and a CrO_3 peak around 49.4° appeared at higher Cr content. Contrary to the results seen in the Fe-containing films, the intensity of the CeO_2 buffer layer peak decreased significantly for films with higher Cr contents in spite of using the same CeO_2/YSZ buffer layer across the substrate. It appears that the Cr reduced the CeO_2 buffer layer during film growth. According to Ellingham−Richardson diagrams, CeO_2 is more stable than MnO and Cr_2O_3, which are themselves more stable than FeO, CoO, and NiO,[38] so one might expect CeO_2 to remain stable in contact with Cr. Other factors related to the

interfacial free energy, the strain energy, and the non-equilibrium deposition process therefore need to be considered to explain the oxygen transfer from CeO_2 to Cr_2O_3. In STCr deposited from a single target,[13] reduction of the CeO_2 was not observed, presumably because there was no excess Cr present.

The films all showed strong STCr (110) and (200) peaks characteristic of double-epitaxial films. As the Cr content increased, the (100):(110) peak ratio decreased and the peaks shifted toward lower angles, corresponding to an increase in the out-of-plane lattice parameters of the STCr films. The out-of-plane lattice parameter increased gradually from 3.922 Å to 3.972 Å as the Cr content increased from 15% to 30%, consistent with the replacement of Ti^{4+} with Cr with mixed valence, similar to the behavior of STCr deposited from single targets.[13]

The decrease of CeO_2 peak intensity also occurred in films prepared by CPLD from STO and MnO targets (Figure 7 panels d, e, and f). The Mn content was relatively low, and the films consisted primarily of perovskite structure STM with additional Mn oxide peaks increasing with the Mn content of the film. Unlike the STO/Cr_2O_3 case, the STM (*h*00) peaks shifted to higher angles with increasing Mn content. The out-of-plane lattice parameter decreased slightly from 3.910 Å to 3.901 Å as the Mn content increased from 3% to 19%. The out-of-plane lattice parameters were similar to bulk STO and much smaller than those of STF or STCr thin films which suggested that the STM films were not in a highly strained state.

None of the films made from STO/Cr_2O_3 and STO/MnO targets had room temperature ferromagnetism. We previously reported that Cr^{3+} and Cr^{6+} ions are present in vacuum-deposited STCr films, which are not magnetoelastic[13] so provide no mechanism for stabilizing the magnetization in strained films. For the samples with Mn, Mn^{2+} (high spin) and Mn^{4+} ions in octahedral sites are also not magnetoelastic, although Mn^{2+} (low spin) and Mn^{3+} ions are, so the presence of magnetoelastic anisotropy in STM depends on both the strain state and the valence and placement of the Mn ions. In the case of Mn ions in $SrTiO_3$, Mn^{2+} (ionic radius 0.83 Å) and Mn^{4+} ions substitute in the Sr^{2+} (1.18 Å) and Ti^{4+} sites, respectively, in materials made in a reducing atmosphere.[39,40] The opportunities for distribution of Mn on different sites could explain why the films grown here were not in highly strained states, which would preclude significant anisotropy even if magnetoelastic ions were present.

5. STN Films from STO and NiO Targets. We finally turn to the case of Ni grown by CPLD using STO and NiO targets. Films grown from the NiO target alone on the same buffer layer and under the same deposition condition of 650 °C and high vacuum showed NiO and metallic Ni peaks. The nickel oxide film had a weak isotropic magnetic hysteresis (not shown) with a coercivity of 100 Oe and a saturation magnetization of ~10 emu/cm^3. This magnetic response is attributed to metallic Ni nanoparticles or to defects in the NiO, which is antiferromagnetic in bulk.[41,42]

The CPLD films were 70−85 nm thick and had roughness below 1 nm. Small Ni and Ni_2O_3 peaks appeared in addition to the majority STN perovskite peaks (Figure 8 panels a, b, and c). The peak around 44.4° corresponding to metallic Ni (111) appeared for films with 39% Ni and increased as the Ni content increased, while the STN (*h*00) peaks decreased and shifted to higher angles. The out-of-plane lattice parameter calculated from the (100) peak of STN decreased linearly from 3.924 Å to 3.917 Å as the Ni content changed from 30% to 49%. The out-of-plane lattice parameters were larger than those of bulk material[12] which is consistent with the STN films being under in-plane compressive strain.

The CPLD films showed qualitatively different magnetic hysteresis compared to the film from the NiO target, with an out-of-plane anisotropy and a higher magnetization, Figure 8 panels d and e. Figure 8 f shows the out-of-plane saturation magnetization and the coercivity as a function of Ni content. The coercivity increased from 30 Oe at 30% Ni to 800 Oe at 49% Ni, and the magnetization increased from 45 emu/cm^3 to 130 emu/cm^3 over the same range.

In this system, metallic Ni is unlikely to account entirely for the ferromagnetism and anisotropy. From its bulk magnetization (485 emu/cm^3), the samples would need to contain 12−20% volume fraction of metallic Ni to provide the magnetization observed in the films, but the XRD peaks for metallic Ni suggest a much smaller fraction. In addition, Ni nanoparticles would not provide the strong anisotropy observed in the films. Measurements of field cooled/zero field cooled magnetization vs temperature showed no peak characteristic of a blocking temperature for superparamagnetic nanoparticles, as seen in other systems such as Ni-implanted ZnO.[43] It seems likely, therefore, that the magnetism originated from the STN phase, with a possible contribution from metallic Ni particles. Ni^{4+} (high spin) or Ni^{3+} in the STN are magnetoelastic and could provide the source of the room temperature magnetism.

■ CONCLUSIONS

CPLD based on the sequential ablation of submonolayer ceramic targets was successful in synthesizing a range of transition metal substituted epitaxial perovskite-structured films on Si substrates. The composition of the film as a function of distance along the substrate fits well to a linear combination of the compositions of the targets. In the STF system, films made combinatorially from pairs of perovskite targets (STO/SFO or STO/STF42.5) formed perovskite-structured STF films with similar microstructure and lattice parameter to STF made from single targets, except at the highest Fe content where the use of CPLD suppressed the formation of spinel phases seen in single-target deposition. In both CPLD and single-target deposition, STF films showed a room temperature ferromagnetism with a strong out-of-plane anisotropy attributed to magnetoelastic effects. This shows that CPLD is a good process for making oxide films with a composition gradient which have comparable structural and magnetic properties to those of films made from a single target.

CPLD was also used to make films from STO/transition metal oxide target pairs, in which the amount of transition metal is greater than the amount in stoichiometric substituted STO. This led to the formation of multiphase films consisting of epitaxial substituted STO films with additional phases of γ-Fe_2O_3 or Fe_3O_4 and FeO, Cr oxides, Mn oxides, and Ni metal and Ni oxide in the cases of Fe, Cr, Mn, and Ni oxide targets, respectively. The Fe case is particularly interesting because the STF + γ-Fe_2O_3 films preserve the strong anisotropy of the STF phase while having a much increased saturation magnetization compared to single-phase STF. The Cr- and Mn-containing films are not ferromagnetic at room temperature, but the Ni-containing films have a strong out-of-plane anisotropy which is attributed mainly to a STN perovskite phase. CPLD is therefore shown to be a convenient process for synthesis of complex oxide perovskite films or of multiphase oxide films which may

have useful magnetic and potentially ferroelectric and multiferroic properties and which can be integrated on Si substrates for device applications.

■ ASSOCIATED CONTENT

Supporting Information

Comparison of saturation magnetic moments measured at room temperature for several types of transition metal substituted $SrTiO_3$. This material is available free of charge via the Internet at http://pubs.acs.org.

■ AUTHOR INFORMATION

Corresponding Author

*E-mail: caross@mit.edu.

Funding

This work was supported by the National Science Foundation, Samsung, DARPA, and the Nanoelectronics Research Initiative.

■ ACKNOWLEDGMENTS

The authors are grateful to Dr. Youngman Jang and Seungha Yoon for assistance in AFM and MFM analysis and thoughtful discussion.

■ REFERENCES

(1) Eerenstein, W.; Mathur, N. D.; Scott, J. F. Multiferroic and magnetoelectric materials. *Nature* **2006**, *442*, 759−765.

(2) Majumdar, P.; Littlewood, P. B. Dependence of magnetoresistivity on charge-carrier density in metallic ferromagnets and doped magnetic semiconductors. *Nature* **1998**, *395*, 479−481.

(3) Rao, C. N. R.; Cheetham, A. K. Giant Magnetoresistance, Charge-Ordering, and Related Aspects of Manganates and Other Oxide Systems. *Adv. Mater.* **1997**, *9*, 1009−1017.

(4) Mckee, R. A.; Walker, F. J.; Chisholm, M. F. Crystalline Oxides on Silicon: The First Five Monolayers. *Phys. Rev. Lett.* **1998**, *81*, 3014−3017.

(5) Grupp, D. E.; Goldman, A. M. Giant Piezoelectric Effect in Strontium Titanate at Cryogenic Temperatures. *Science* **1997**, *276*, 392−394.

(6) Jun, S.; Kim, Y. S.; Lee, J.; Kim, Y. W. Dielectric properties of strained (Ba,Sr)TiO_3 thin films epitaxially grown on Si with thin yttria-stabilized zirconia buffer layer. *Appl. Phys. Lett.* **2001**, *78*, 2542−2544.

(7) Yamada, T.; Wakiya, N.; Shinozaki, K.; Mizutani, N. Epitaxial growth of $SrTiO_3$ on CeO_2/yttria-stabilized zirconia/Si (001) with TiO_2 atomic layer by pulsed-laser deposition. *Appl. Phys. Lett.* **2003**, *83*, 4815−4817.

(8) Vispute, R. D.; Narayan, J.; Dovidenko, K.; Jagannadham, K.; Parikh, N.; Suvkhanov, A.; Budai, J. D. Heteroepitaxial structures of $SrTiO_3$/TiN on Si (100) by in situ pulsed laser deposition. *J. Appl. Phys.* **1996**, *80*, 6720−6724.

(9) Migita, S.; Sakai, S. Epitaxial structure $SrTiO_3$ ⟨011⟩ on Si ⟨001⟩. *J. Appl. Phys.* **2001**, *89*, 5421−5424.

(10) Kim, H.-S.; Bi, L.; Dionne, G. F.; Ross, C. A. Magnetic and magneto-optical properties of Fe-doped $SrTiO_3$ films. *Appl. Phys. Lett.* **2008**, *93*, 092506−1−3.

(11) Bi, L.; Kim, H.-S.; Dionne, G. F.; Ross, C. A. Structure, magnetic properties and magnetoelastic anisotropy in epitaxial $Sr(Ti_{1-x}Co_x)O_3$ films. *New J. Phys.* **2010**, *12*, 043044.

(12) Phuong, D. T. T.; Hong, L. V.; Minh, N. V. $SrTi_{1-x}Ni_xO_3$ nanoparticles: synthesis and characterisation. *Int. J. Nanotechnol.* **2011**, *8*, 312−323.

(13) Kim, D. H.; Bi, L.; Jiang, P.; Dionne, G. F.; Ross, C. A. Magnetoelastic effects in $Sr(Ti_{1-x}M_x)O_3$ (M = Fe, Co, or Cr) epitaxial thin films. *Phys. Rev B.* **2011**, *84*, 014416−1−9.

(14) Martin, L. W.; Chu, Y.-H.; Ramesh, R. Advanced in the growth and characterization of magnetic, ferroelectric, and multiferroic oxide thin films. *Mater. Sci. Eng. R.* **2010**, *68*, 89−133.

(15) Christen, H. M.; Silliman, S. D.; Harshavardhan, K. S. Continuous compositional-spread technique based on pulsed-laser deposition and applied to the growth of epitaxial films. *Rev. Sci. Instrum.* **2001**, *72*, 2673−2678.

(16) Venimadhav, A.; Yates, K. A.; Blamire, M. G. Scanning Raman Spectroscopy for Characterizing Compositionally Spread Films. *J. Comb. Chem.* **2005**, *7*, 85−89.

(17) Yamada, Y. F.; Ohtomo, A.; Kawasaki, M. Parallel syntheses and thermoelectric properties of Ce-doped $SrTiO_3$ thin films. *Appl. Surf. Sci.* **2007**, *254*, 768−771.

(18) Joshi, U. S.; Itaka, K.; Matsumoto, Y.; Koinuma, H. Combinatorial fabrication and magnetic properties of homoepitaxial Co and Li co-doped NiO thin-film nanostructures. *J. Magn. Magn. Mater.* **2009**, *321*, 3595−3599.

(19) Clevenger, T. R. Effect of Fe^{4+} in the system $SrFeO_3$−$SrTiO_3$. *J. Am. Ceram. Soc.* **1963**, *46*, 207−210.

(20) Muenstermann, R.; Menke, T.; Dittmann, R.; Waser, R. Coexistence of Filamentary and Homogeneous Resistive Switching in Fe-Doped $SrTiO_3$ Thin-Film Memristive Devices. *Adv. Mater.* **2010**, *22*, 4819−4822.

(21) Choi, G. M.; Tuller, H. L.; Goldschmidt, D. Electronic-transport behavior in single-crystalline $Ba_{0.03}Sr_{0.97}TiO_3$. *Phys. Rev B.* **1986**, *34*, 6972−6979.

(22) Rothschild, A.; Menesklou, W.; Tuller, H. L.; Riffée, E. I. Electronic Structure, Defect Chemistry, and Transport Properties of $SrTi_{1-x}Fe_xO_{3-y}$ Solid Solutions. *Chem. Mater.* **2006**, *18*, 3651−3659.

(23) Norton, D. P.; Theodoropoulou, N. A.; Hebard, A. F.; Budai, J. D.; Boatner, L. A.; Pearton, S. J.; Wilson, R. G. Properties of Mn-Implanted $BaTiO_3$, $SrTiO_3$, and $KTaO_3$. *Electrochem. Solid-State Lett.* **2003**, *6*, G19−G21.

(24) Zhang, S.-Y.; Lin, Y.-H.; Nan, C.-W.; Zhao, R. Magnetic and Electrical Properties of (Mn, La)-Codoped $SrTiO_3$ Thin Films. *J. Am. Ceram. Soc.* **2008**, *91*, 3263−3266.

(25) Vorobiev, A.; Rundqvist, P.; Khamchane, K.; Gevorgian, S. Microwave properties of $SrTiO_3$/$SrRuO_3$/CeO_2/YSZ heterostructure on low-resistivity silicon. *J. Eur. Ceram. Soc.* **2003**, *23*, 2711−2715.

(26) Lei, C. H.; Tendeloo, G.; Van.; Siegert, M.; Schubert, J. Buchal, Ch. Structural investigation of the epitaxial yittria-stabilized zirconia films deposited on (001) silicon by laser ablation. *J. Cryst. Growth.* **2001**, *222*, 558−564.

(27) Vasiliev, A. L.; van Tendeloo, G.; Amelinckx, A.; Boikov, Yu.; Olsson, E.; Ivanov, Z. Structural aspect of $YBa_2Cu_3O_{7-x}$ films on Si with complex barrier layers. *Phys. C* **1995**, *244*, 373−388.

(28) Pereira, S.; Correia, M. R.; Pereira, E.; O'Donnel, K. P.; Alves, E.; Sequeira, A. D.; Franco, N. Interpretation of double X-ray diffraction peaks from InGaN layers. *Appl. Phys. Lett.* **2001**, *79*, 1432−1434.

(29) Kim, H.-S.; Bi, L.; Paik, H.; Yang, D.-J.; Park, Y. C.; Dionne, G. F.; Ross, C. A. Self-Assembled Single-Phase Perovskite Nanocomposite Thin Films. *Nano Lett.* **2010**, *10*, 597−602.

(30) Gan, Q.; Rao, R. A.; Eom, C. B.; Garrett, J. L.; Lee, M. Direct measurement of strain effects on magnetic and electrical properties of epitaxial $SrRuO_3$ thin films. *Appl. Phys. Lett.* **1998**, *72*, 978−980.

(31) Tepper, T.; Ilievski, F.; Ross, C. A.; Zaman, T. R.; Ram, R. J.; Sung, S. Y.; Stadler, B. J. H. Magneto-optical properties of iron oxide films. *J. Appl. Phys.* **2003**, *93*, 6948−6950.

(32) Tepper, T.; Ross, C. A. Pulsed laser deposition of iron oxide films. *J. Appl. Phys.* **2002**, *91*, 4453−4456.

(33) Kneller, E. F.; Hqwig, R. The Exchange-Spring Magnet: A New Material Principle for Permanent Magnets. *IEEE Trans. Magn.* **1991**, *24*, 3588−3600.

(34) Fullerton, E. E.; Jiang, J. S.; Bader, S. D. Hard/soft magnetic heterostructures: model exchange-spring magnets. *J. Magn. Magn. Mater.* **1999**, *200*, 392−404.

(35) Wagner, C. D.; Riggs, W. M.; Davis, L. E.; Moulder, J. F.; Muilenberg, G. E. *Handbooks of X-ray photoelectron spectroscopy.*; Perkin-Elmer Corporation: Eden Prairie, MN, 1978; pp 76−77.

(36) Kanatani, H.; Kume, H.; Matsui, T. Magnetic properties of $SrTiO_3$-buffered Ba $(Fe_{0.2}Zr_{0.8})O_{3-\delta}$ films on Si (001) substrates. *J. Appl. Phys.* **2009**, *105*, 07D907-1-3.
(37) Matsui, T.; Taketani, E.; Sato, R.; Morii, K. Origin of the leakage current in Zr-substituted magneto-dielectric $BaFeO_{3-\delta}$single-crystal films on (001) $SrTiO_3$ substrates. *J. Phys. D: Appl. Phys.* **2007**, *40*, 6066−6070.
(38) Darken, L. S.; Gurry, R. W. *Physical Chemistry of Metals*; McGraw Hill: New York, 1953; p 349.
(39) Tkach, A.; Vilarinho, P. M.; Kholkin, A. L. Dependence of dielectric properties of manganese-doped strontium titanate ceramics on sintering atmosphere. *Acta. Mater.* **2006**, *54*, 5385−5391.
(40) Badalyan, A. G.; Syrnikov, P. P.; Azzoni, C. B.; Galinetto, P.; Mozzati, M. C.; Rosa, J.; Trepakov, V. A.; Jastrabik, L. Manganese oxide nanoparticles in $SrTiO_3$:Mn. *J. Appl. Phys.* **2008**, *104*, 033917-1−033917-4.
(41) Zhang, W.-B.; Yu, N.; Yu, W.-Y.; Tang, B.-Y. Stability and magnetism of vacancy in NiO: a GGA+U study. *Eur. Phys. J. B* **2008**, *64*, 153−158.
(42) Yi, J. B.; Ding, J.; Feng, Y. P.; Peng, G. W.; Chow, G. M.; Kawazoe, Y.; Lie, B. H.; Yin, J. H.; Thongmee, S. Size-dependent magnetism and spin-glass behavior of amorphous NiO bulk, cluster, and nanocrystals: Experiment and first-principles calculations. *Phys. Rev. B* **2007**, *76*, 224402-1−224402-5.
(43) Zhou, S.; Potzger., K.; Borany, J.; von; Grötzschel, R.; Skorupa, W.; Helm, M.; Fassbender, J. Crystallographically oriented Co and Ni nanocrystals inside ZnO formed by ion implantation and postannealing. *Phys. Rev. B.* **2008**, *77*, 035209-1−035209-12.